Guanglei Wu[1]
e-mail: gwu@m-tech.aau.dk

Shaoping Bai
e-mail: shb@m-tech.aau.dk

Jørgen A. Kepler
e-mail: jk@m-tech.aau.dk

Department of Mechanical and Manufacturing Engineering, Aalborg University, Fibigerstræde 16, DK-9220 Aalborg East, Denmark

Stéphane Caro
Institut de Recherche en Communications et Cybernétique de Nantes, France
e-mail: stephane.caro@irccyn.ec-nantes.fr

Error Modeling and Experimental Validation of a Planar 3-PPR Parallel Manipulator With Joint Clearances

This paper deals with the error modeling and analysis of a 3-PPR planar parallel manipulator with joint clearances. The kinematics and the Cartesian workspace of the manipulator are analyzed. An error model is established with considerations of both configuration errors and joint clearances. Using this model, the upper bounds and distributions of the pose errors for this manipulator are established. The results are compared with experimental measurements and show the effectiveness of the error prediction model. [DOI: 10.1115/1.4007487]

1 Introduction

The planar parallel manipulators (PPMs) with three identical kinematic chains are special parallel manipulators (PMs), whose motion is confined in a plane. For this type of PM, the error modeling and analysis are important for both design and control in order to utilize the PMs potential of high accuracy in applications.

A number of works on accuracy analysis of parallel mechanisms can be found in the literature. Ryu and Cha derived a volumetric error model and a total error transformation matrix from a differential inverse kinematic equation, which includes possible kinematic error sources [1]. Liu et al. reported an approach of geometric error modeling for lower mobility manipulators by explicitly separating the compensatable and uncompensatable error sources affecting the pose accuracy [2]. Yu et al. reported a simple geometric approach to computing the exact local maximum position and orientation error by illustrating several different types of 3-dof planar parallel robots [3]. Briot and Bonev proposed a method based on geometric approach for detailed error analysis of a fully parallel robot with three translations and one rotation that brings valuable understanding of the error amplification problem [4].

Research focusing on the influence of joint clearances has been reported too. Lin and Chen proposed a homogeneous error transformation matrix to assess the effects of joint clearances on pose errors [5]. Ting et al. presented a simple method to identify the worst position and direction errors due to the joint clearance of linkages and manipulators, which offers a geometrical model to warranty the precision of a mechanism [6]. Fogarasy and Smith utilized the derivatives of the closure equations to obtain a first order approximation of the output error, which is called the Jacobian method [7]. Regarding the errors of universal and spherical joints due to clearances as a part of link errors, Lim et al. [8] analyzed the dynamic error of a cubic parallel mechanism by using its forward kinematics. Castelli and Venanzi applied the virtual work principle to determine the position of the end-effector when a given external load is applied [9,10]. Meng et al. proposed an error model of PMs subject to joint clearances by formulating the error prediction model as a standard convex optimization problem [11], of which the constraints are formed through a set of inequalities about the joint clearances. A general error prediction model considering joint clearances was established for serial and parallel manipulators by means of differential screw theory in Ref. [12]. It was used to analyze the kinematic sensitivity of a 3-PPR parallel manipulator to joint clearances in Ref. [13]. Wei and Simaan proposed an approach for designing inexpensive planar parallel robots with prescribed backlash-free workspace by using preloaded flexible joints to replace the passive joints [14]. Among the sources of errors, the influence of assembly and manufacturing errors and actuation errors can be eliminated as indicated in Refs. [5,15–17] by calibration, except joint clearances due to its low repeatability. It means that the pose errors due to joint clearances require a special consideration. Simple and valid methods of error modeling for PPMs are needed for accuracy analysis.

In this paper, the error analysis of PPMs is studied with consideration of both configuration errors and joint clearances. An error model is established, upon which the maximal error problem was transformed into an optimization problem. The distributions of global maximal pose errors in the prescribed workspace can be formulated effectively. Moreover, the error model based on the joint clearances was validated experimentally. The work was conducted for a novel 3-PPR PPM with a nonsymmetrical base [18], which has a larger workspace and the same level of motion accuracy compared to the traditional symmetrical PPMs.

This paper is organized as follows. The architecture of the manipulator under study is presented in Sec. 2. The kinematics and Cartesian workspace are analyzed in Sec. 3. The error prediction model is established in Sec. 4. Sections 5 and 6 present the experimental validation, in which measured results are compared with the simulations. The work is concluded in Sec. 7.

2 Manipulator Under Study

Figure 1 presents the Computer-Aided Design (CAD) model of the planar 3-PPR parallel manipulator with a rigid equilateral triangle-shape moving platform (MP). Here and throughout this paper, P and R stand for prismatic and revolute joints, respectively. An underlined letter indicates an actuated joint. Each leg is driven by a *CAL* 35 actuator, a high resolution linear motor built with an encoder of 5 μm accuracy from SMAC company [19]. A THK linear guide of model HRW17 is used as the active prismatic joint P. A linear bearing mounted on the slider of the linear guide is used as the passive prismatic joint in each leg. The ball joints in Fig. 1 are preloaded, of which joint clearance does not exist. For the built physical prototype, the end-effector can also be replaced by a disk-shape MP with ordinary revolute joints to couple the three legs, but this introduces more error sources due to the clearances between the pin and the hole of the revolute joint.

[1]Corresponding author.

Contributed by the Mechanisms and Robotics Committee of ASME for publication in the Journal of Mechanisms and Robotics. Manuscript received August 15, 2011; final manuscript received August 6, 2012; published online September 17, 2012. Assoc. Editor: Delun Wang.

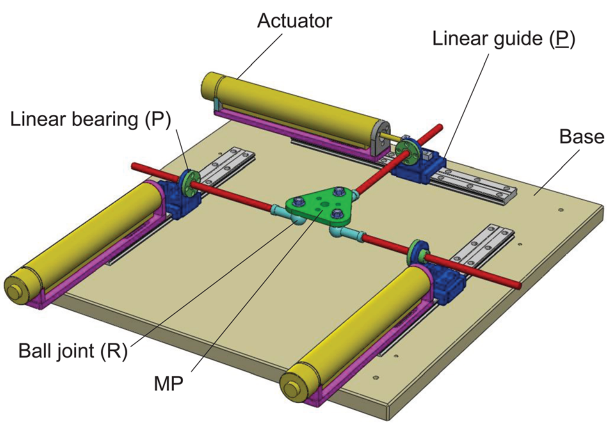

Fig. 1 CAD model of a 3-PPR PPM

The parameterization of the 3-PPR PPM is illustrated in Fig. 2, where A_i, $i = 1, 2, 3$, are fixed points on the base. The x-axis of the coordinate system $\mathcal{F}_b$ is parallel to the segment A_1A_2. The origin P of the coordinate system $\mathcal{F}_p$ is located at the geometric center of the triangle $\Delta D_1D_2D_3$ on the moving platform and the X-axis is parallel to the segment D_1D_2, where D_i, $i = 1, 2, 3$, are the centers of the revolute joints. The translational and orientational displacements of the MP are denoted by $\mathbf{p}$ and ϕ, where $\mathbf{p} = [x, y]$, x and y being the Cartesian coordinates of point P in $\mathcal{F}_b$.

3 Kinematic Modeling of the 3-PPR PPM

The kinematic modeling of the manipulator is described in this section. The workspace and singularities of the manipulator are also analyzed based on its closure equations.

From the closed-loop kinematic chains $O - A_i - B_i - C_i - D_i - P - O$ shown in Fig. 2, the position vector of point P can be expressed in $\mathcal{F}_b$ as follows:

$$\mathbf{p} = a_i\mathbf{h}_i + s_i\mathbf{u}_i + d_i\mathbf{v}_i + l_i\mathbf{w}_i + r_i\mathbf{k}_i, \;\; i = 1, 2, 3 \tag{1}$$

with

$$\mathbf{h}_i = \begin{bmatrix}\cos\alpha_i \\ \sin\alpha_i\end{bmatrix}, \quad \mathbf{u}_i = \begin{bmatrix}\cos\beta'_i \\ \sin\beta'_i\end{bmatrix}, \quad \mathbf{v}_i = \begin{bmatrix}\cos\gamma'_i \\ \sin\gamma'_i\end{bmatrix},$$
$$\mathbf{w}_i = \begin{bmatrix}\cos\theta'_i \\ \sin\theta'_i\end{bmatrix}, \quad \mathbf{k}_i = \begin{bmatrix}\cos(\phi + \psi_i) \\ \sin(\phi + \psi_i)\end{bmatrix}$$

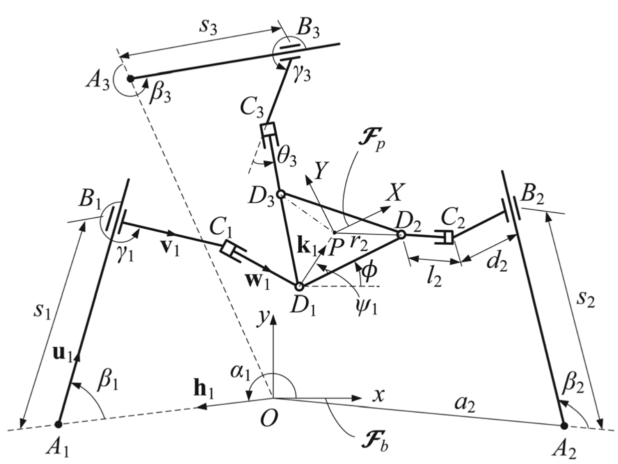

Fig. 2 Parameterization of the 3-PPR PPM

and

$$\beta'_i = \alpha_i + \beta_i, \gamma'_i = \alpha_i + \beta_i + \gamma_i, \theta'_i = \alpha_i + \beta_i + \gamma_i + \theta_i$$

The inverse kinematics of the manipulator can be derived from Eq. (1)

$$s_i = (\mathbf{w}_i^T\mathbf{E}\mathbf{u}_i)^{-1}\mathbf{w}_i^T\mathbf{E}(\mathbf{p} - a_i\mathbf{h}_i - d_i\mathbf{v}_i - r_i\mathbf{k}_i) \tag{2a}$$
$$l_i = (\mathbf{u}_i^T\mathbf{E}\mathbf{w}_i)^{-1}\mathbf{u}_i^T\mathbf{E}(\mathbf{p} - a_i\mathbf{h}_i - d_i\mathbf{v}_i - r_i\mathbf{k}_i) \tag{2b}$$

matrix $\mathbf{E}$ is the right angle rotation matrix defined as

$$\mathbf{E} = \begin{bmatrix}0 & -1 \\ 1 & 0\end{bmatrix}$$

Equation (1) establishes a system of six equations. The forward displacements can be solved by virtue of analytical method. The velocity expression of the manipulator can be derived from Eq. (1) as below

$$\mathbf{A}\begin{bmatrix}\dot{\mathbf{p}} \\ \dot{\phi}\end{bmatrix} = \mathbf{B}\dot{\mathbf{s}} \tag{3}$$

with

$$\mathbf{A} = \begin{bmatrix}\mathbf{w}_1^T\mathbf{E}^T & -r_1\mathbf{w}_1^T\mathbf{k}_1 \\ \mathbf{w}_2^T\mathbf{E}^T & -r_2\mathbf{w}_2^T\mathbf{k}_2 \\ \mathbf{w}_3^T\mathbf{E}^T & -r_3\mathbf{w}_3^T\mathbf{k}_3\end{bmatrix} \tag{4a}$$
$$\mathbf{B} = \mathrm{diag}\left[\mathbf{w}_1^T\mathbf{E}^T\mathbf{u}_1 \quad \mathbf{w}_2^T\mathbf{E}^T\mathbf{u}_2 \quad \mathbf{w}_3^T\mathbf{E}^T\mathbf{u}_3\right] \tag{4b}$$
$$\dot{\mathbf{s}} = [\dot{s}_1 \quad \dot{s}_2 \quad \dot{s}_3]^T \tag{4c}$$

where $\mathbf{A}$ and $\mathbf{B}$ are the forward and backward Jacobians of the manipulator, respectively. The kinematic Jacobian matrix $\mathbf{J}$ of the manipulator takes the form

$$\mathbf{J} = \mathbf{A}^{-1}\mathbf{B} \tag{5}$$

Matrix $\mathbf{A}$ is singular, i.e., the manipulator reaches a parallel singularity, when $\phi = \pm\pi/2$. Matrix $\mathbf{B}$ is never singular, namely, the manipulator is free of serial singularity.

The reachable area of the moving platform with a constant orientation can be obtained geometrically by means of searching method [13,18], where the inverse kinematics model, namely, Eqs. (2a) and (2b), establish a system of 12 inequations by virtue of the joint motion limits to formulate the motion constraints of the MP. With the parameters shown in Table 1 and $r_i = r = 30$ mm, $a_i = 192.34$ mm, $i = 1, 2, 3$, constant-orientation Cartesian workspaces for three orientations of the MP are illustrated in Fig. 3.

4 Error Modeling of a 3-PPR PPM

Here, a methodology introduced in Ref. [20] was used to derive the error model of the MP pose with regard to variations in the actuated and passive joints as well as in the Cartesian coordinates of points A_i, B_i, C_i, and D_i, $i = 1, 2, 3$.

Table 1 The design parameters of the 3-PPR PPM

i	α_i(rad)	$\beta\prime_i$(rad)	γ'_i, θ'_i(rad)	ψ_i(rad)	d_i(mm)
1	−2.781	$\pi/2$	0	$\pi/6$	114
2	−0.360	$\pi/2$	π	$5\pi/6$	27
3	1.751	0	$-\pi/2$	$3\pi/2$	42

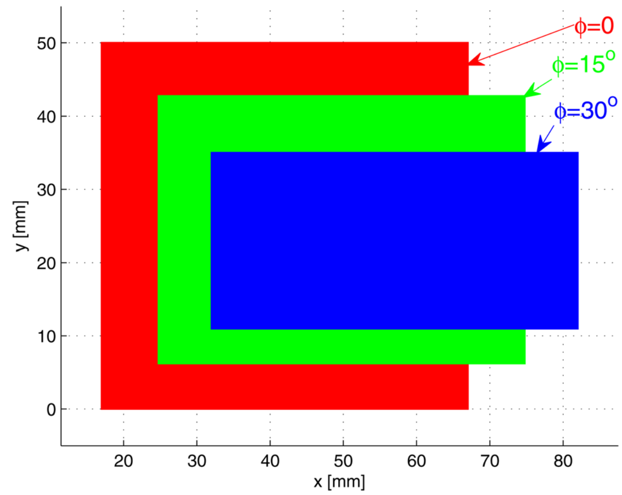

Fig. 3 Constant-orientation workspaces

4.1 Error Prediction Model. The clearance in the revolute joint between the ith leg and the moving platform is characterized by the small displacement between points D_i and point D_i' as shown in Fig. 4. Upon differentiation of Eq. (1), we obtain the positioning error of point P with respect to each leg

$$\begin{aligned}\delta\mathbf{p} &= \delta a_i\mathbf{h}_i + a_i\delta\alpha_i\mathbf{E}\mathbf{h}_i + \delta s_i\mathbf{u}_i + s_i\delta\beta_i'\mathbf{E}\mathbf{u}_i + \delta d_i\mathbf{v}_i \\ &\quad + d_i\delta\gamma_i'\mathbf{E}\mathbf{v}_i + \delta l_i\mathbf{w}_i + l_i\delta\theta_i'\mathbf{E}\mathbf{w}_i + \delta\rho_i\mathbf{n}_i \\ &\quad + \delta r_i\mathbf{k}_i + r_i(\delta\phi + \delta\psi_i)\mathbf{E}\mathbf{k}_i,\ i = 1,2,3\end{aligned} \tag{6}$$

where

$$\begin{aligned}\delta\beta_i' &= \delta\alpha_i + \delta\beta_i \\ \delta\gamma_i' &= \delta\alpha_i + \delta\beta_i + \delta\gamma_i \\ \delta\theta_i' &= \delta\alpha_i + \delta\beta_i + \delta\gamma_i + \delta\theta_i\end{aligned} \tag{7}$$

where $\delta\mathbf{p}$ and $\delta\phi$ are the positioning and orientation errors of the moving platform expressed in $\mathcal{F}_b$, respectively. Moreover, $\delta a_i, \delta\alpha_i, \delta s_i, \delta\beta_i, \delta d_i, \delta\gamma_i, \delta l_i, \delta\theta_i, \delta r_i$, and $\delta\psi_i$ denote variations in the geometric parameters illustrated in Fig. 4. In addition, $\delta\rho_i$ is a small displacement between point D_i and point $D\prime_i$ due to the clearance in the ith revolute joint and $\mathbf{n}_i = [\cos\varphi_i, \sin\varphi_i]^T$, as illustrated in Fig. 5(*b*). Substituting Eqs. (7) into (6) and eliminating the idle variation δl_i lead to

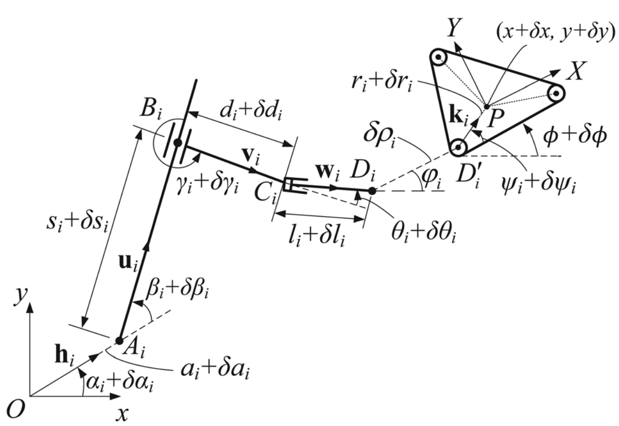

Fig. 4 Parameterization of the *i*th leg

$$\begin{aligned}\mathbf{w}_i^T\mathbf{E}^T\delta\mathbf{p} &= \delta a_i\mathbf{w}_i^T\mathbf{E}^T\mathbf{h}_i + \delta\alpha_i\left[\mathbf{w}_i^T(a_i\mathbf{h}_i + s_i\mathbf{u}_i + d_i\mathbf{v}_i) + l_i\right] \\ &\quad + \delta s_i\mathbf{w}_i^T\mathbf{E}^T\mathbf{u}_i + \delta\beta_i\left[\mathbf{w}_i^T(s_i\mathbf{u}_i + d_i\mathbf{v}_i) + l_i\right] \\ &\quad + \delta d_i\mathbf{w}_i^T\mathbf{E}^T\mathbf{v}_i + \delta\gamma_i(d_i\mathbf{w}_i^T\mathbf{v}_i + l_i) + l_i\delta\theta_i \\ &\quad + \delta\rho_i\mathbf{w}_i^T\mathbf{E}^T\mathbf{n}_i + \delta r_i\mathbf{w}_i^T\mathbf{E}^T\mathbf{k}_i + r_i(\delta\phi + \delta\psi_i)\mathbf{w}_i^T\mathbf{k}_i\end{aligned} \tag{8}$$

Equation (8) can be cast in vector form

$$\begin{aligned}\mathbf{A}\begin{bmatrix}\delta x\\ \delta y\\ \delta\phi\end{bmatrix} &= \mathbf{H}_a\begin{bmatrix}\delta a_1\\ \delta a_2\\ \delta a_3\end{bmatrix} + \mathbf{H}_\alpha\begin{bmatrix}\delta\alpha_1\\ \delta\alpha_2\\ \delta\alpha_3\end{bmatrix} + \mathbf{B}\begin{bmatrix}\delta s_1\\ \delta s_2\\ \delta s_3\end{bmatrix} \\ &\quad + \mathbf{H}_\beta\begin{bmatrix}\delta\beta_1\\ \delta\beta_2\\ \delta\beta_3\end{bmatrix} + \mathbf{H}_d\begin{bmatrix}\delta d_1\\ \delta d_2\\ \delta d_3\end{bmatrix} + \mathbf{H}_\gamma\begin{bmatrix}\delta\gamma_1\\ \delta\gamma_2\\ \delta\gamma_3\end{bmatrix} \\ &\quad + \mathbf{H}_\theta\begin{bmatrix}\delta\theta_1\\ \delta\theta_2\\ \delta\theta_3\end{bmatrix} + \mathbf{H}_\rho\begin{bmatrix}\delta\rho_1\\ \delta\rho_2\\ \delta\rho_3\end{bmatrix} \\ &\quad + \mathbf{H}_r\begin{bmatrix}\delta r_1\\ \delta r_2\\ \delta r_3\end{bmatrix} + \mathbf{H}_\psi\begin{bmatrix}\delta\psi_1\\ \delta\psi_2\\ \delta\psi_3\end{bmatrix}\end{aligned} \tag{9}$$

where all $\mathbf{H}_q, q \in \{a, \alpha, \beta, d, \gamma, \theta, \rho, r, \psi\}$, are 3×3 matrices as given in Appendix A. Moreover, assuming that $\mathbf{A}$ is nonsingular, the multiplication of both sides of Eq. (9) by $\mathbf{A}^{-1}$ leads to

$$\begin{aligned}\begin{bmatrix}\delta x\\ \delta y\\ \delta\phi\end{bmatrix} &= \mathbf{J}_a\begin{bmatrix}\delta a_1\\ \delta a_2\\ \delta a_3\end{bmatrix} + \mathbf{J}_\alpha\begin{bmatrix}\delta\alpha_1\\ \delta\alpha_2\\ \delta\alpha_3\end{bmatrix} + \mathbf{J}\begin{bmatrix}\delta s_1\\ \delta s_2\\ \delta s_3\end{bmatrix} + \mathbf{J}_\beta\begin{bmatrix}\delta\beta_1\\ \delta\beta_2\\ \delta\beta_3\end{bmatrix} \\ &\quad + \mathbf{J}_d\begin{bmatrix}\delta d_1\\ \delta d_2\\ \delta d_3\end{bmatrix} + \mathbf{J}_\gamma\begin{bmatrix}\delta\gamma_1\\ \delta\gamma_2\\ \delta\gamma_3\end{bmatrix} + \mathbf{J}_\theta\begin{bmatrix}\delta\theta_1\\ \delta\theta_2\\ \delta\theta_3\end{bmatrix} \\ &\quad + \mathbf{J}_\rho\begin{bmatrix}\delta\rho_1\\ \delta\rho_2\\ \delta\rho_3\end{bmatrix} + \mathbf{J}_r\begin{bmatrix}\delta r_1\\ \delta r_2\\ \delta r_3\end{bmatrix} + \mathbf{J}_\psi\begin{bmatrix}\delta\psi_1\\ \delta\psi_2\\ \delta\psi_3\end{bmatrix}\end{aligned} \tag{10}$$

with

$$\mathbf{J}_q = \mathbf{A}^{-1}\mathbf{H}_q, q \in \{a, \alpha, \beta, d, \gamma, \theta, \rho, r, \psi\} \tag{11}$$

where $\mathbf{J}$ and $\mathbf{J}_q$ are the sensitivity coefficients of the MP pose of the manipulator to variations in terms of coordinates of each link [20]. It will be more useful to find the sensitivity coefficients in the coordinates of all joint positions, namely, points A_i, B_i, C_i, and D_i. By making use of

$$\begin{bmatrix}\delta a_{ix}\\ \delta a_{iy}\end{bmatrix} = \begin{bmatrix}\cos\alpha_i & -a_i\sin\alpha_i\\ \sin\alpha_i & a_i\cos\alpha_i\end{bmatrix}\begin{bmatrix}\delta a_i\\ \delta\alpha_i\end{bmatrix} \tag{12a}$$

$$\begin{bmatrix}\delta b_{ix}\\ \delta b_{iy}\end{bmatrix} = \begin{bmatrix}\cos\beta_i & -s_i\sin\beta_i\\ \sin\beta_i & s_i\cos\beta_i\end{bmatrix}\begin{bmatrix}0\\ \delta\beta_i\end{bmatrix} \tag{12b}$$

$$\begin{bmatrix}\delta c_{ix}\\ \delta c_{iy}\end{bmatrix} = \begin{bmatrix}\cos\gamma_i & -d_i\sin\gamma_i\\ \sin\gamma_i & d_i\cos\gamma_i\end{bmatrix}\begin{bmatrix}\delta d_i\\ \delta\gamma_i\end{bmatrix} \tag{12c}$$

$$\begin{bmatrix}\delta d_{ix}\\ \delta d_{iy}\end{bmatrix} = \begin{bmatrix}\cos\psi_i & -r_i\sin\psi_i\\ \sin\psi_i & r_i\cos\psi_i\end{bmatrix}\begin{bmatrix}\delta r_i\\ \delta\psi_i\end{bmatrix} \tag{12d}$$

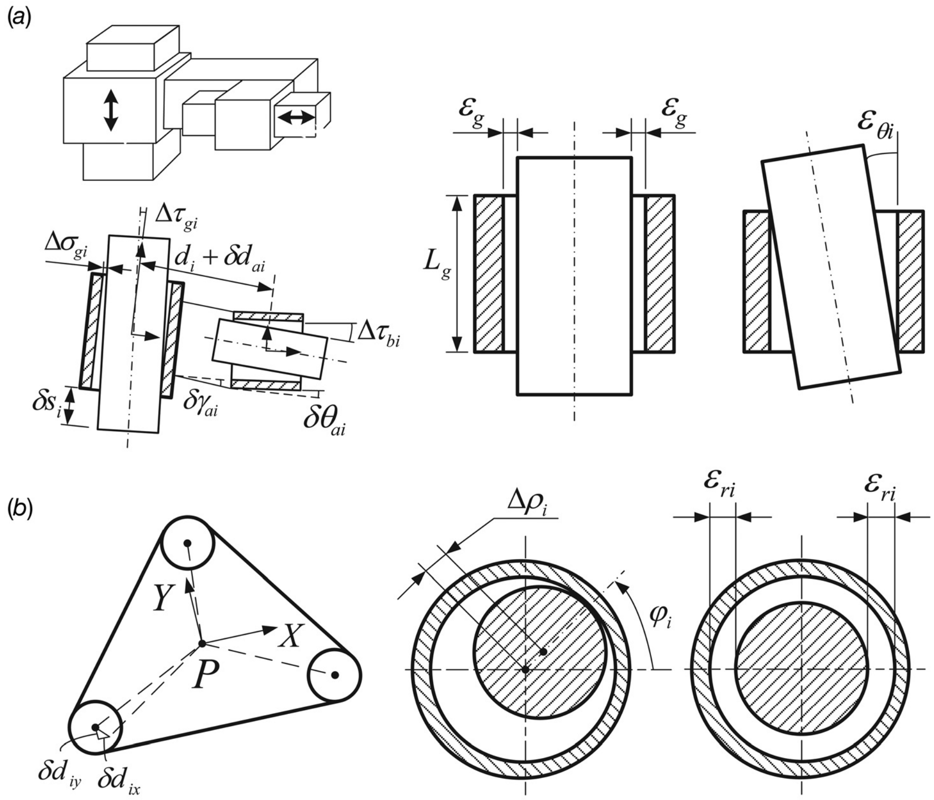

Fig. 5 Geometric errors and joint clearances related to the *i*th leg: (*a*) prismatic joint and (*b*) revolute joint

Equation (10) is transformed as

$$\begin{bmatrix}\delta\mathbf{p}\\ \delta\phi\end{bmatrix} = \mathbf{J}\begin{bmatrix}\delta s_1\\ \delta s_2\\ \delta s_3\end{bmatrix} + \mathbf{J}_\theta\begin{bmatrix}\delta\theta_1\\ \delta\theta_2\\ \delta\theta_3\end{bmatrix} + \mathbf{J}_\rho\begin{bmatrix}\delta\rho_1\\ \delta\rho_2\\ \delta\rho_3\end{bmatrix} + \mathbf{J}_A\begin{bmatrix}\delta a_{1x}\\ \delta a_{1y}\\ \delta a_{2x}\\ \delta a_{2y}\\ \delta a_{3x}\\ \delta a_{3y}\end{bmatrix} + \mathbf{J}_B\begin{bmatrix}\delta b_{1x}\\ \delta b_{1y}\\ \delta b_{2x}\\ \delta b_{2y}\\ \delta b_{3x}\\ \delta b_{3y}\end{bmatrix} + \mathbf{J}_C\begin{bmatrix}\delta c_{1x}\\ \delta c_{1y}\\ \delta c_{2x}\\ \delta c_{2y}\\ \delta c_{3x}\\ \delta c_{3y}\end{bmatrix} + \mathbf{J}_D\begin{bmatrix}\delta d_{1x}\\ \delta d_{1y}\\ \delta d_{2x}\\ \delta d_{2y}\\ \delta d_{3x}\\ \delta d_{3y}\end{bmatrix} \tag{13}$$

where δa_{ix} and δa_{iy} (δb_{ix} and $\delta b_{iy}, \delta c_{ix}$, and δc_{iy}, resp.) are the positioning errors of point A_i (B_i, C_i, resp.), $i = 1, 2, 3$, along x- and y-axes, namely, the variations in the Cartesian coordinates. Notice that δd_{ix} and δd_{iy} denote the positioning errors of points $D\prime_i$ along X- and Y-axes, namely, the variations in the Cartesian coordinates of D'_i. The 3×6 matrices $\mathbf{J}_A, \mathbf{J}_B, \mathbf{J}_C$, and $\mathbf{J}_D$ can be found in Appendix A. Equation (13) can be written in the following form:

$$\begin{bmatrix}\delta\mathbf{p}\\ \delta\phi\end{bmatrix} = \mathbf{J}_{\text{err}}\boldsymbol{\delta}_{\text{var}} \tag{14}$$

where

$$\mathbf{J}_{\text{err}} = [\,\mathbf{J} \quad \mathbf{J}_\theta \quad \mathbf{J}_\rho \quad \mathbf{J}_A \quad \mathbf{J}_B \quad \mathbf{J}_C \quad \mathbf{J}_D\,] \tag{15a}$$

$$\delta_{\text{var}} = \begin{bmatrix}\delta\mathbf{s}^T & \delta\boldsymbol{\theta}^T & \delta\boldsymbol{\rho}^T & \delta\mathbf{a}^T & \delta\mathbf{b}^T & \delta\mathbf{c}^T & \delta\mathbf{d}^T\end{bmatrix}^T \tag{15b}$$

with

$$\delta\mathbf{s} = \begin{bmatrix}\delta s_1\\ \delta s_2\\ \delta s_3\end{bmatrix}, \quad \delta\boldsymbol{\theta} = \begin{bmatrix}\delta\theta_1\\ \delta\theta_2\\ \delta\theta_3\end{bmatrix}, \quad \delta\boldsymbol{\rho} = \begin{bmatrix}\delta\rho_1\\ \delta\rho_2\\ \delta\rho_3\end{bmatrix}, \quad \delta\mathbf{e} = \begin{bmatrix}\delta\mathbf{e}_1\\ \delta\mathbf{e}_2\\ \delta\mathbf{e}_3\end{bmatrix}$$

$$\delta\mathbf{e}_i = \begin{bmatrix}\delta e_{ix} & \delta e_{iy}\end{bmatrix}^T, \quad e \in \{a, b, c, d\}, \quad i = 1, 2, 3$$

where $\mathbf{J}_{\text{err}}$ is the global sensitivity Jacobian matrix and $\boldsymbol{\delta}_{\text{var}}$ is a vector containing all variations. For a given posture, all submatrices except $\mathbf{J}_\rho$ are known.

4.2 Modeling the Joint Clearances.

Figure 5 illustrates the assembly errors and clearances in the prismatic and revolute joints. $\delta d_{ai}, \delta\beta_i, \delta\gamma_{ai}$ and $\delta\theta_{ai}$, $i = 1, 2, 3$, are the assembly errors while δd_{ix} and δd_{iy} correspond to the manufacturing errors. Moreover, $\Delta\sigma_{gi}, \Delta\tau_{gi}, \Delta\tau_{bi}$ and $\Delta\rho_i$ are the displacements due to joint clearances. Then, we have

$$\delta d_i = \delta d_{ai} + \Delta\sigma_{gi}, \delta\gamma_i = \delta\gamma_{ai} + \Delta\tau_{gi}, \delta\theta_i = \delta\theta_{ai} + \Delta\tau_{bi}$$

The errors due to the clearances in the linear guides are characterized by the following constraints [11]:

$$-2\varepsilon_{gi} \le L_g\Delta\tau_{gi} + 2\Delta\sigma_{gi} \le 2\varepsilon_{gi} \tag{16a}$$

$$-2\varepsilon_{gi} \le -L_g\Delta\tau_{gi} + 2\Delta\sigma_{gi} \le 2\varepsilon_{gi} \tag{16b}$$

where ε_{gi} specifies the lateral clearance and L_g is the length of the linear guide block. Alternatively, the errors in the linear bearing are constrained by the following condition:

$$-\varepsilon_{\theta i} \leq \Delta\tau_{bi} \leq \varepsilon_{\theta i} \tag{17}$$

where $\varepsilon_{\theta i}$ is the upper bound of $\Delta\tau_{bi}$. Figure 5(*a*) demonstrates the tolerances of the linear guides and bearing. The clearances in the three revolute joints meet the following constraint:

$$0 \leq \Delta\rho_i \leq \varepsilon_{ri}, \ i = 1, 2, 3 \tag{18}$$

where ε_{ri} is the range of variations $\Delta\rho_i$ due to the joint clearance shown in Fig. 5(*b*).

4.3 Maximum Pose Errors of the Moving Platform With Joint Clearances. The pose errors due to the assembly and actuation errors can be determined from Eq. (14), while the errors due to joint clearances will be solved by virtue of an optimization method. When only joint clearances are considered, the relationship between the pose errors and joint clearances becomes:

$$\begin{bmatrix} \delta\mathbf{p} \\ \delta\phi \end{bmatrix} = \mathbf{J}^c_{err}\boldsymbol{\delta}^c_{var} \tag{19}$$

with

$$\mathbf{J}^{\mathrm{c}}_{\mathrm{err}} = [\,\mathbf{J}_\theta \quad \mathbf{J}_d \quad \mathbf{J}_\gamma \quad \mathbf{J}_\rho\,]_{3\times 12} \rightarrow \equiv \begin{bmatrix} \mathbf{J}^{\mathrm{c}}_{\mathrm{err},x} \\ \mathbf{J}^{\mathrm{c}}_{\mathrm{err},y} \\ \mathbf{J}^{\mathrm{c}}_{\mathrm{err},\phi} \end{bmatrix} \tag{20a}$$

$$\boldsymbol{\delta}^c_{var} = [\,\Delta\tau_{b1} \quad \Delta\tau_{b2} \quad \Delta\tau_{b3} \quad \Delta\sigma_{g1} \quad \Delta\sigma_{g2} \quad \Delta\sigma_{g3} \quad \Delta\tau_{g1} \quad \Delta\tau_{g2} \quad \Delta\tau_{g3} \quad \Delta\rho_1 \quad \Delta\rho_2 \quad \Delta\rho_3\,]^T \tag{20b}$$

where $\mathbf{J}^c_{\mathrm{err},x}, \mathbf{J}^c_{\mathrm{err},y}, \mathbf{J}^c_{\mathrm{err},\phi}$ are three 1×12 submatrices corresponding to the first, the second, and the third rows of $\mathbf{J}^c_{\mathrm{err}}$. The maximum positioning error along x-axis, y-axis, and the maximum orientation error of the MP, namely, $\delta x_{\max}, \delta y_{\max}$ and $\delta\phi_{\max}$, can be obtained by solving the following optimization problem:

$$\begin{aligned} \delta\zeta^2_{\max} &\equiv \max\left(\mathbf{J}^c_{\mathrm{err},\zeta}\boldsymbol{\delta}^c_{\mathrm{var}}\right)^2 \text{ for } x, y, \phi \in \Omega \\ \mathrm{ST} \quad & -2\varepsilon_{gi} \leq L_g\Delta\tau_{gi} + 2\Delta\sigma_{gi} \leq 2\varepsilon_{gi} \\ & -2\varepsilon_{gi} \leq -L_g\Delta\tau_{gi} + 2\Delta\sigma_{gi} \leq 2\varepsilon_{gi} \\ & -\varepsilon_{\theta i} \leq \Delta\tau_{bi} \leq \varepsilon_{\theta i} \\ & 0 \leq \Delta\rho_i \leq \varepsilon_{ri} \\ & 0 \leq \varphi_i \leq 2\pi \\ & i = 1, 2, 3, \zeta \in \{x, y, \phi\} \end{aligned} \tag{21}$$

where Ω denotes the Cartesian workspace of the manipulator defined in Sec. 3. Optimization problem of Eq. (21) aims at finding separately the maximum positioning errors along the x-axis and y-axis and the maximum orientation error of the moving platform. Note that the three maximum errors are subject to the same constraints, hence, the optimization problems are written in a generalized form.

The maximum positioning error $\delta p_{\max}$ is obtained by solving the following optimization problem:

$$\begin{aligned} \delta p^2_{\max} &\equiv \max\left(\mathbf{J}^c_{\mathrm{err},p}\boldsymbol{\delta}^c_{\mathrm{var}}\right)^T\left(\mathbf{J}^c_{\mathrm{err},p}\boldsymbol{\delta}^c_{\mathrm{var}}\right) \text{ for } x, y, \phi \in \Omega \\ \mathrm{ST} \quad & -2\varepsilon_{gi} \leq L_g\Delta\tau_{gi} + 2\Delta\sigma_{gi} \leq 2\varepsilon_{gi} \\ & -2\varepsilon_{gi} \leq -L_g\Delta\tau_{gi} + 2\Delta\sigma_{gi} \leq 2\varepsilon_{gi} \\ & -\varepsilon_{\theta i} \leq \Delta\tau_{bi} \leq \varepsilon_{\theta i} \\ & 0 \leq \Delta\rho_i \leq \varepsilon_{ri} \\ & 0 \leq \varphi_i \leq 2\pi \\ & i = 1, 2, 3 \end{aligned} \tag{22}$$

where $\mathbf{J}^c_{\mathrm{err},p} = [\,\mathbf{J}^{c\ T}_{\mathrm{err},x} \quad \mathbf{J}^{c\ T}_{\mathrm{err},y}\,]^T$. The foregoing optimization problems are solved using the MATLAB *fmincon* function. According to the product catalogues, the clearance in the lateral direction of the linear guide is equal to 3μm, namely, $2\varepsilon_{gi} = 2\varepsilon_g = 3\mu$m. As a consequence, the errors due to the linear guides are negligible. δa_{ix} and δa_{iy} are set to zero too. Finally, the maximum position error and the maximum orientation error of the MP can be evaluated from Eqs. (21) and (22) for any configuration of the manipulator by known joint clearances and geometric tolerances.

5 Experimental Setup and Measurement Errors

A main purpose of the work is to experimentally validate the error model developed. To this end, experiments have been conducted in which the position and orientation of the MP were measured with a vision-based system composed of a single Charge-Coupled Device (CCD) camera. The experimental setup is shown in Fig. 6(*a*) and its specifications are given hereafter:

- DVT 554c smart camera with 1280×1024 pixel resolution (7.4μm $\times$ 7.4μm pixels) from Cognex [21] was fixed right above the MP for pose measurements.
- INTELLECT 1.5.1, a vision software from Cognex [22], was used to establish the communication with the camera via data cable as shown in Fig. 6(*b*). The Blobs are used to locate markers on the MP.

With this system, the position and orientation measurement accuracies are 0.01 mm and 0.01 deg, respectively.

5.1 Measurements. Before the measurements, the system was calibrated. A standard calibration paper with markers of 2 cm spacing from Cognex was used to establish the reference frame. The calibration method is described in the INTELLECT 1.5 Guide [22].

5.1.1 Assembly Errors. In measuring configuration error, the first linear guide was used as the y-axis of the reference frame, which means $\delta\beta_1 = 0$. The measurement is illustrated in Fig. 7. Four holes on each linear guide were used as the markers. $\delta\beta_2$ and $\delta\beta_3$ can be obtained by means of the INTELLECT software. Similarly, a perfect regular component with four uniformly distributed holes was used to measure the assembly errors $\delta\gamma_{ai}$ and $\delta\theta_{ai}$ by means of face to face alignments. The measured assembly errors are listed in Table 2.

5.1.2 Joint Clearances. Figure 8 illustrates the method used to measure the clearance in the linear bearing. Pushing the right end of the shaft back and forth and measuring the difference of the two counts δ_{LB}, the value of δ_{LB}/L_s was adopted as the bound of angular clearance. For the revolute joint clearances, the diameters of the joint pin and the cylinder were measured, respectively. The half value of the difference of the two measurements was adopted as the clearance bound. The bounds of the joint clearances were found as

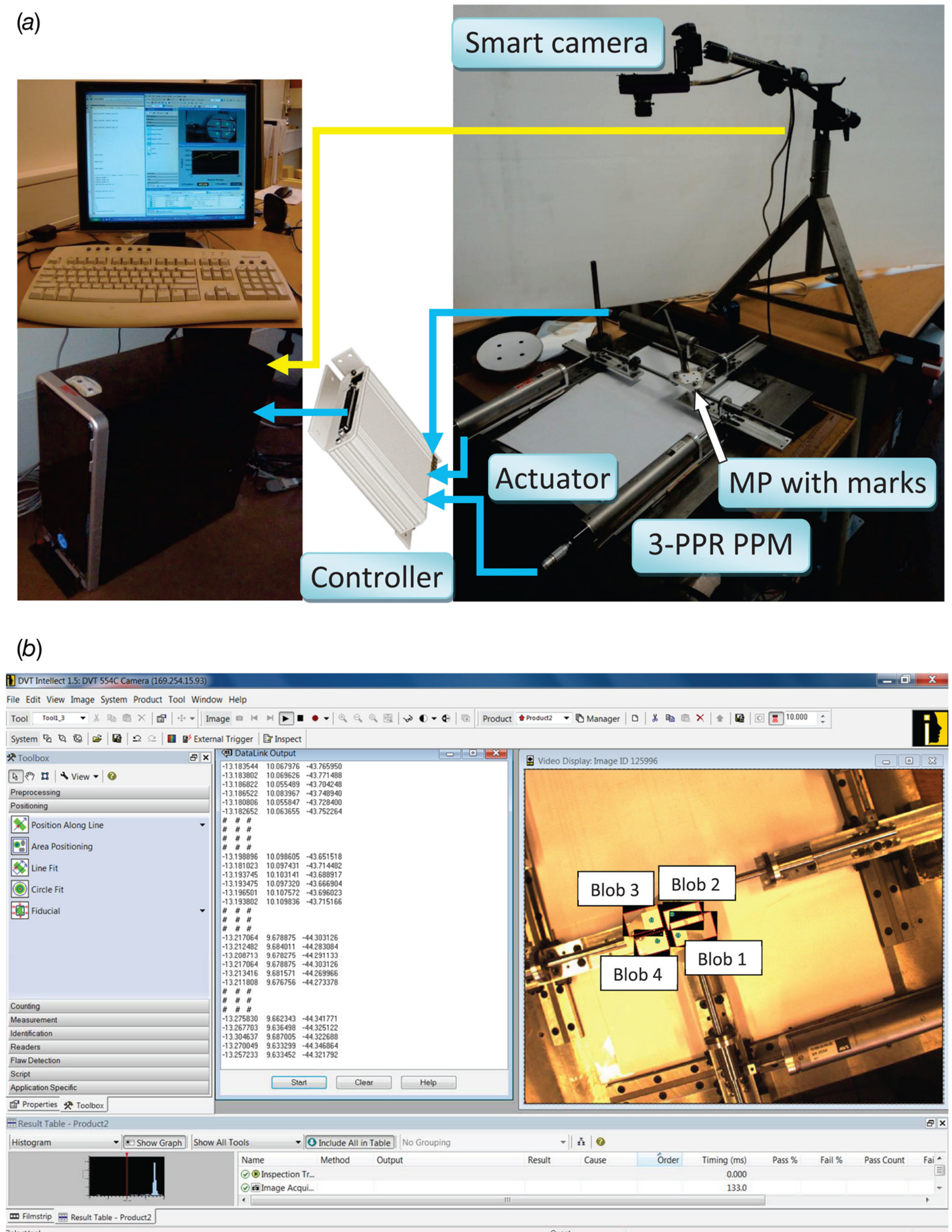

Fig. 6 A vision-based system for the moving platform pose measurement: (*a*) experimental setup and (*b*) measurement interface

$$\varepsilon_{\theta i} = \varepsilon_{\theta} = 0.0012 \text{ rad}, \quad i = 1, 2, 3$$

$$\varepsilon_{r1} = 0.039 \text{ mm}, \quad \varepsilon_{r2} = 0.036 \text{ mm}, \quad \varepsilon_{r3} = 0.037 \text{ mm}$$

5.2 Pose Errors of MP. The measurements were conducted with two cases:

- Case 1: a case with only clearances in the passive prismatic joints
- Case 2: a case with clearances in both passive prismatic and revolute joints

The two cases were physically implemented with two different shapes for the moving platform in Sec. 2, respectively, namely, the equilateral triangle MP (Δ-shape MP) and the disk-shape MP ($\bigcirc$-shape MP), which are associated with Cases 1 and 2. We first fixed on the MP a calibration paper with 2×2 marks of 2 cm separation in case 1. Then, $i \times j$ uniformly distributed points were measured throughout the Cartesian workspace of the manipulator.

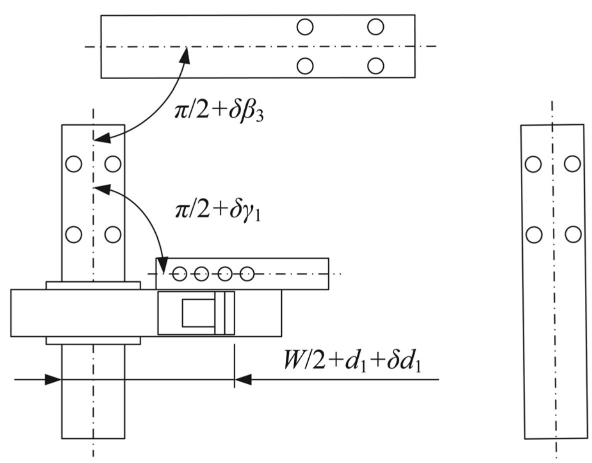

Fig. 7 Measurement of the assembly errors

Table 2 Measurements of assembly errors

i	$\delta\beta_i$(rad)	$\delta\gamma_{ai}$(rad)	$\delta\theta_{ai}$(rad)	δd_{ai}(mm)
1	0	0.016	−0.028	−0.12
2	0.014	0.020	−0.022	−0.08
3	−0.010	0.020	0.034	0.15

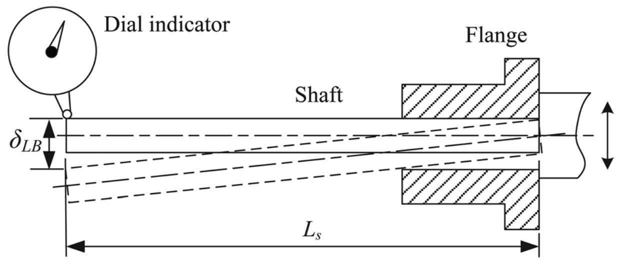

Fig. 8 Measurement of the angular clearance in the linear bearing

During the measurements, the actuators were locked to eliminate the errors in the actuators. At the (i, j) point, the MP was slightly pushed bidirectionally along the x-axis, y-axis, and rotated about the z-axis, respectively. The corresponding readings were noted as $(x, y, \phi)^{ij}_{+t}$ and $(x, y, \phi)^{ij}_{-t}, t \in \{x, y, r\}$, respectively. The measured positioning and orientation errors at the (i, j) point are defined as:

$$\delta x^{ij} = \max\left\{x^{ij}_{+t}, x^{ij}_{-t}\right\} - \min\left\{x^{ij}_{+t}, x^{ij}_{-t}\right\} \tag{23a}$$

$$\delta y^{ij} = \max\left\{y^{ij}_{+t}, y^{ij}_{-t}\right\} - \min\left\{y^{ij}_{+t}, y^{ij}_{-t}\right\} \tag{23b}$$

$$\delta\phi^{ij} = \max\left\{\phi^{ij}_{+t}, \phi^{ij}_{-t}\right\} - \min\left\{\phi^{ij}_{+t}, \phi^{ij}_{-t}\right\} \tag{23c}$$

$$\delta p^{ij} = \max\left\{\delta p^{ij}_t\right\}, \delta p^{ij}_t = \sqrt{(x^{ij}_{+t} - x^{ij}_{-t})^2 + (y^{ij}_{+t} - y^{ij}_{-t})^2} \tag{23d}$$

6 Results and Discussion

In this section, the predicted maximum pose errors from the model and measured errors from the experiments are presented and compared.

6.1 Error Distributions for Case 1. Figure 6 represents the error distribution of the moving platform for a given orientation $\phi = 0$. Figure 9(a) shows that the simulated $\delta x_{\max}$ is constant for a given y-coordinate and decreases slightly with the y-coordinate. $\delta x_{\max}$ is bounded between 0.196 mm and 0.256 mm, while $\delta y_{\max}$ and $\delta\phi_{\max}$ are both constant, their values being equal to 0.100 mm and 0.221 deg, respectively. The y-coordinate of point P, the geometric center of the MP, and the orientation of the MP depend only on the first and second prismatic actuators because of the partial motion decoupling of the manipulator. Therefore, the maximum position error of the MP along the y-axis and its maximum rotation error occur when $\Delta\tau_{bi}, i = 1, 2$, reach their lower or upper bounds. As a result, both $\delta y_{\max}$ and $\delta\phi_{\max}$ remain constant throughout the Cartesian workspace of the manipulator. From Fig. 9(c), it is apparent that the maximum positioning error $\delta p_{\max}$ of the MP is symmetrical with respect to the x-axis. The root-mean-square deviation (RMSD) values between the simulations and measurements are equal to 50 μm, 30 μm, 51 μm, and 0.057 deg, for δx, δy, δp, and $\delta\phi$, respectively. From Fig. 6, it is noteworthy that there is a good correlation between the measured positioning errors and the simulated ones. On the other hand, the differences between the measured orientation errors of the MP and the

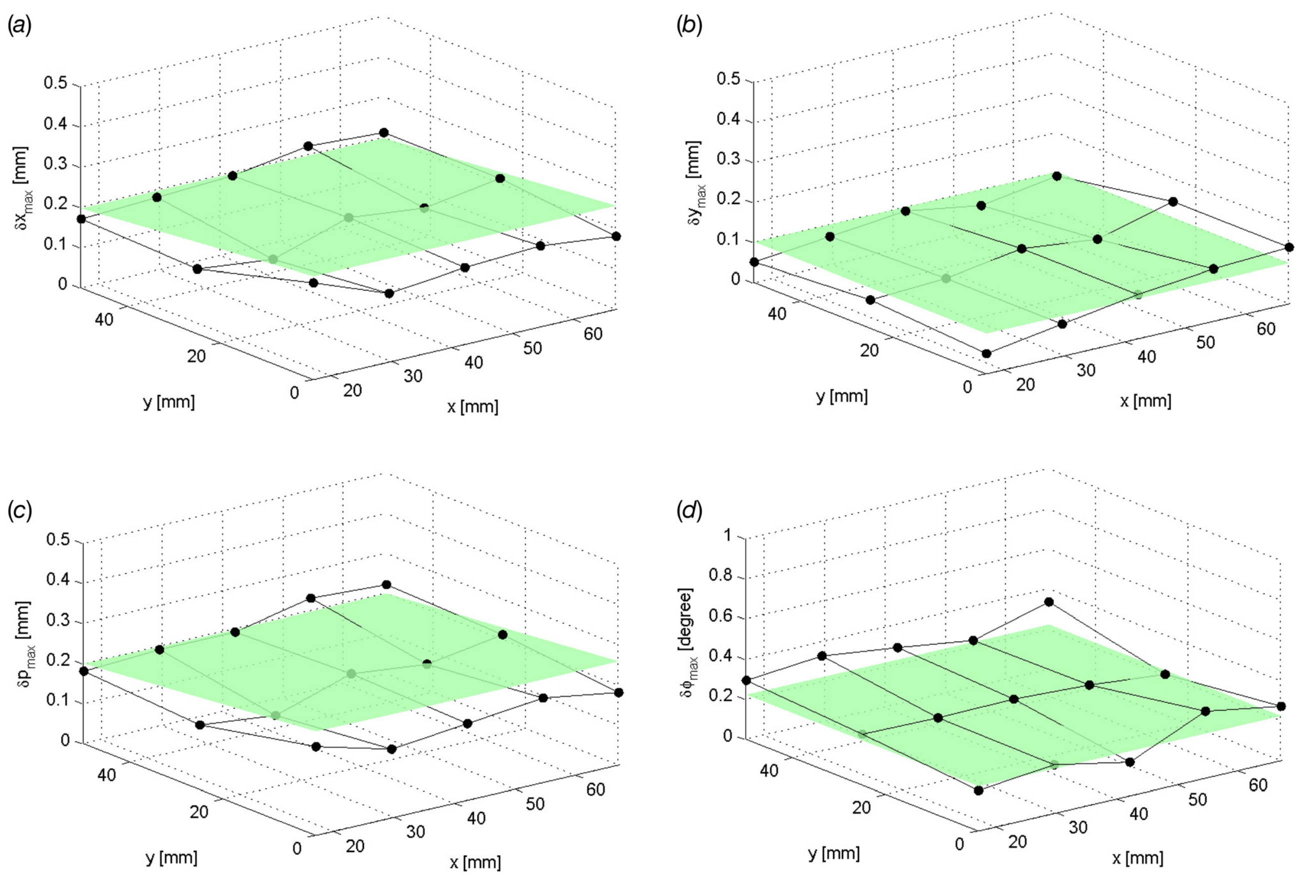

Fig. 9 Comparison of error distributions for case 1 with a constant orientation $\phi = 0$: The solid surface is obtained from simulation while dot points from measurements

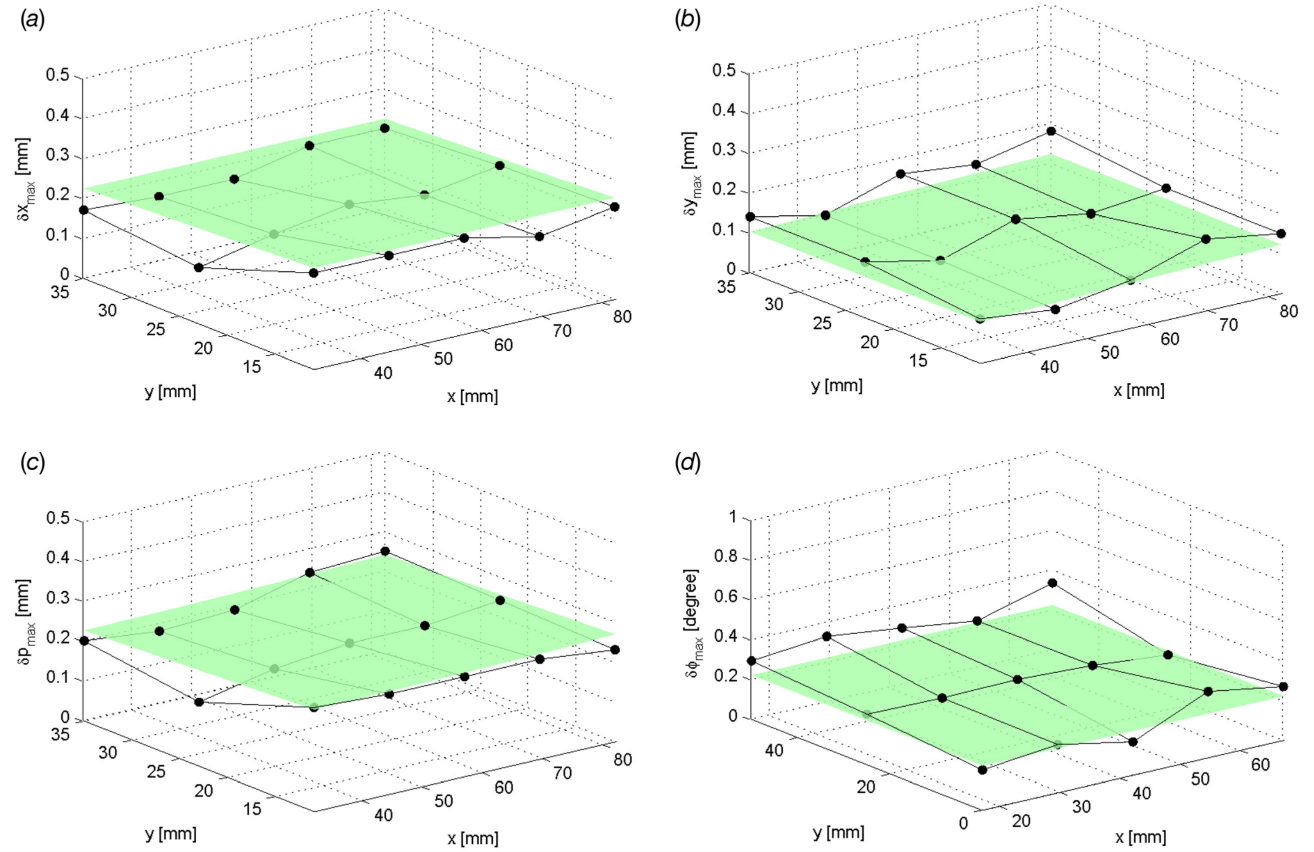

Fig. 10 Comparison of error distributions for case 1 with a constant orientation $\phi = \pi/6$

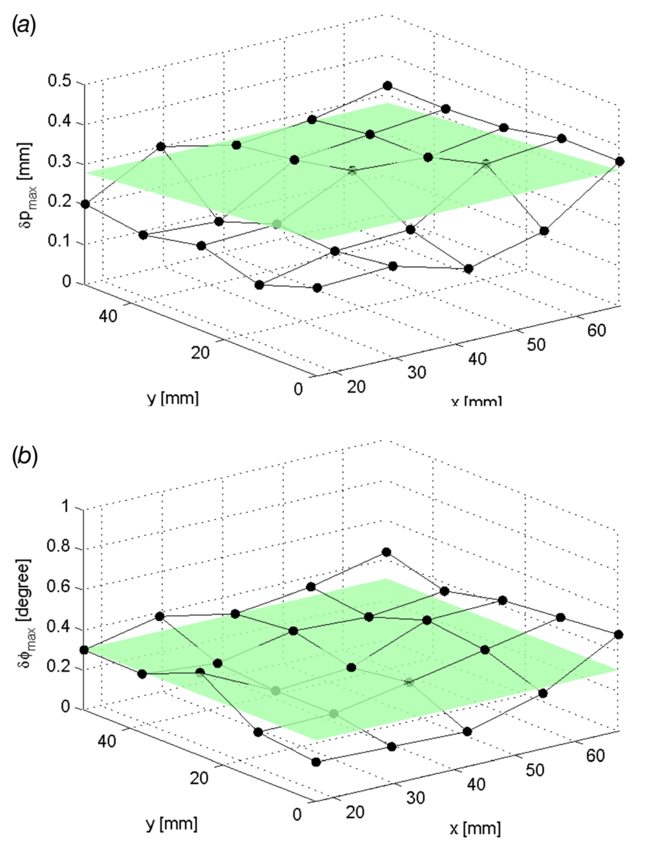

Fig. 11 Comparison of error distributions for case 2 with a constant orientation $\phi = 0$

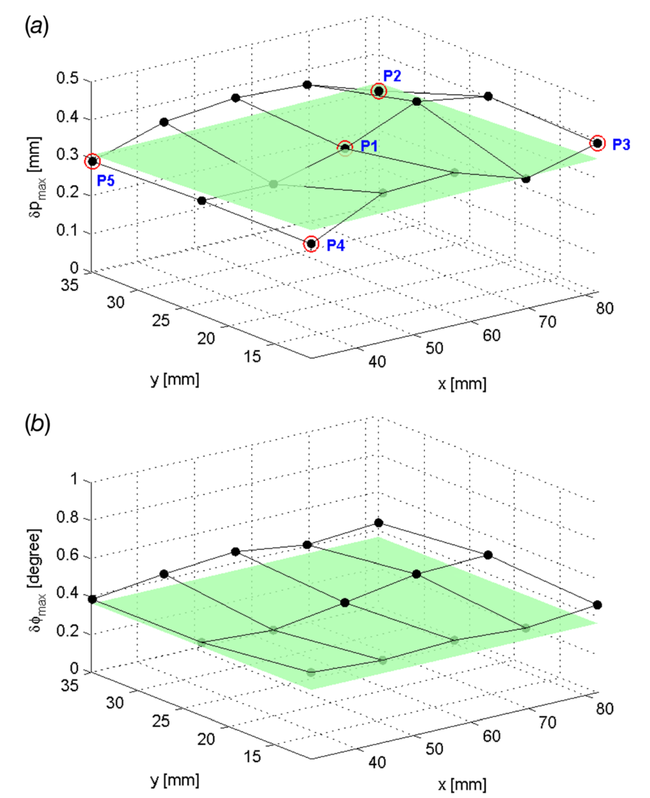

Fig. 12 Comparison of error distributions for case 2 with a constant orientation $\phi = \pi/6$

simulated ones are noticeable. To some extent, this is due to the reason that angular measurement is more sensitive to the random error and influence of environments, etc., than the positional measurement.

The distributions of measured errors with constant orientation $\phi = \pi/6$ are shown in Fig. 10. The simulated $\delta x_{\max}$, as shown in Fig. 10(*a*), varying from 0.224 mm to 0.253 mm, has a distribution similar to that corresponding to $\phi = 0$, while $\delta y_{\max}$ is constant along *y*-axis and increases gradually with the *x*-coordinate (see Fig. 10(*b*)), from 0.103 mm to 0.123 mm. In Fig. 10(*d*), the simulated orientation error $\delta\phi_{\max}$ is constant and is equal to 0.264 deg. The positioning error $\delta p_{\max}$, varying from 0.226 mm to 0.268 mm, increases when the measuring point moves from the upper left corner to the lower right corner throughout the workspace as displayed in Fig. 10(*c*). The RMSD values between the simulations and measurements of $\delta x, \delta y, \delta p$, and $\delta\phi$ are equal to 47 μm, 34 μm, 34 μm, and 0.103 deg, respectively. Therefore, the measurements have a good correlation with the simulations.

6.2 Error Distributions for Case 2. In case 2, both prismatic and revolute joint clearances are considered. The distributions of the maximum pose errors are shown in Figs. 11 and 12. By comparing Figs. 11 to 6, it can be found that the differences between the simulation results and measurements really depend on the orientation of the MP. For $\phi = 0$, the RMSD values between the simulations and measurements are equal to 77 μm, 62 μm, 81 μm, and 0.086 deg, for $\delta x, \delta y, \delta p$, and $\delta\phi$, respectively. Although the difference between the simulations and experiments in Fig. 11(*b*) under the given scale and unit seems larger than the other results, however, the maximum value is around 0.5 deg and the statistical analysis also shows that the difference is acceptable.

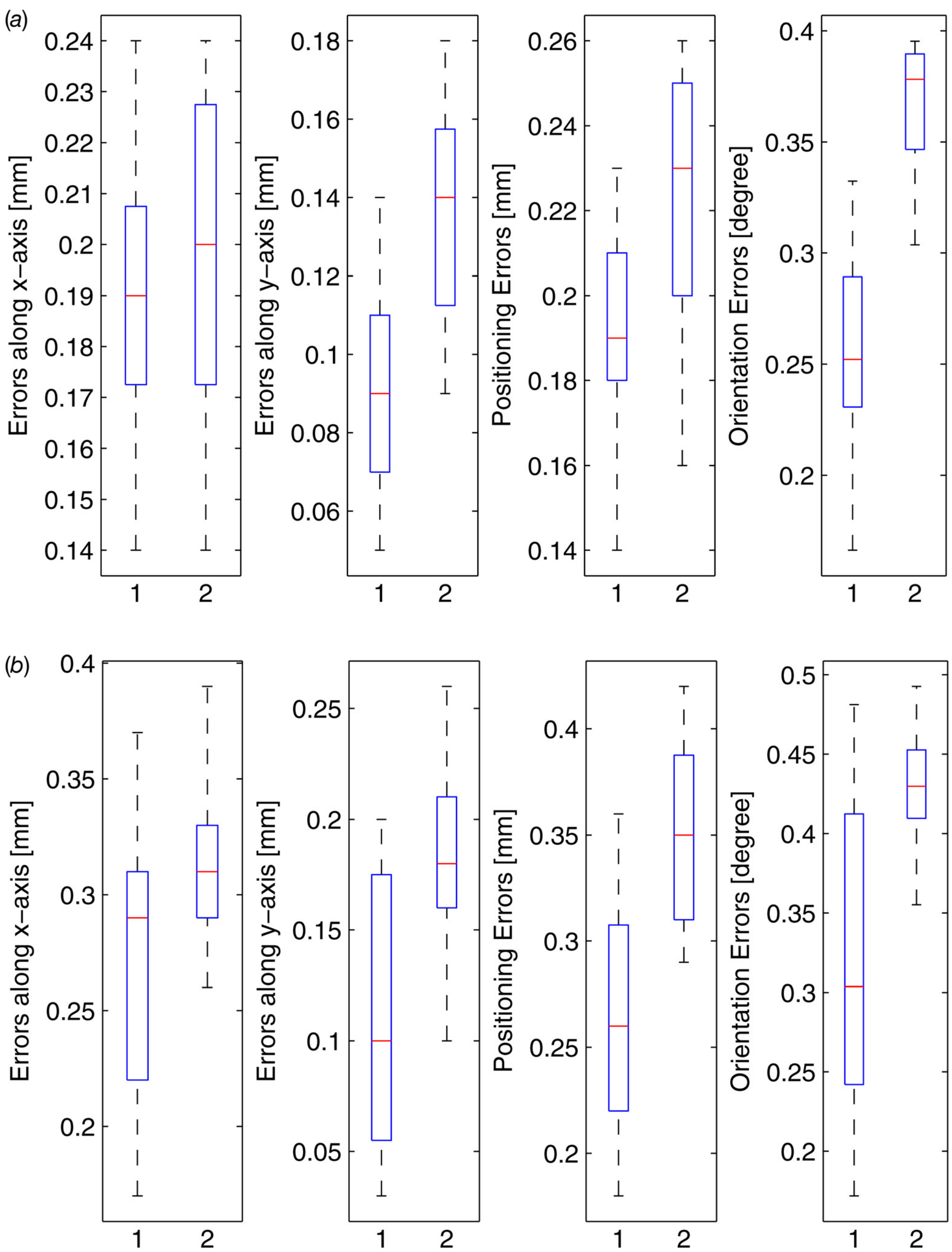

Fig. 13 Boxplot of the measurements for cases 1 and 2. Nos. 1 and 2 of horizontal axes stand for the measurements with constant orientations $\phi = 0$ and $\phi = \pi/6$, respectively.

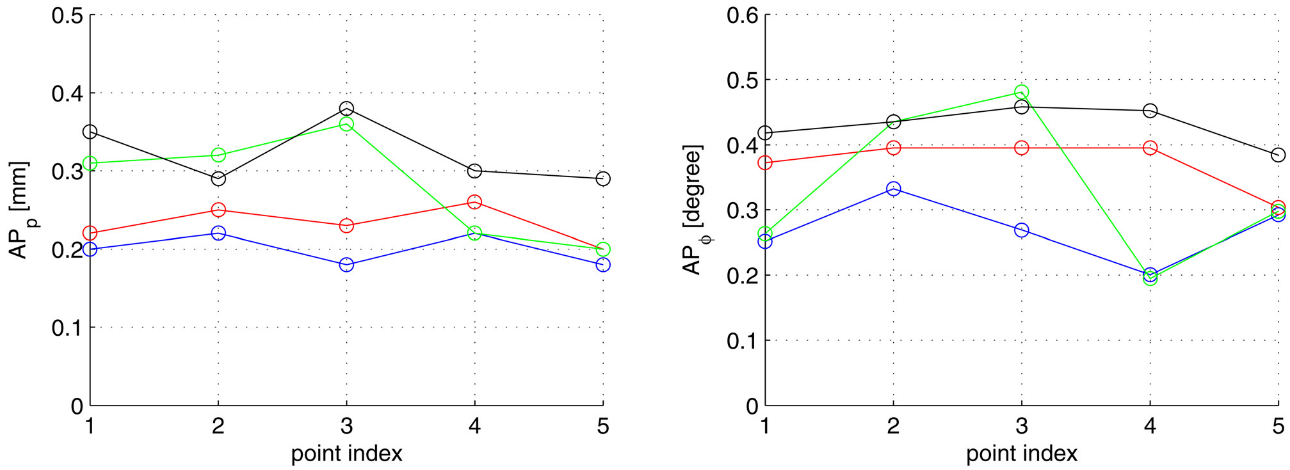

Fig. 14 Position and orientation accuracies at five poses

For $\phi = \pi/6$, the RMSD values between the simulations and measurements of $\delta x, \delta y, \delta p$ and $\delta\phi$, are equal to 26 μm, 36 μm, 34 μm, and 0.063 deg, respectively. Note that the correlation between the simulation results and the measurements is better with $\phi = \pi/6$ than $\phi = 0$.

6.3 Discussion on Measurement Results. As shown in Fig. 13, both for cases 1 and 2, the measurement errors with $\phi = \pi/6$ are larger than that of $\phi = 0$, which agrees with the distributions obtained from simulations. Moreover, the sample standard deviations (SSD) of the measured orientation errors are equal to 0.052, 0.029, 0.086, and 0.034 deg, respectively. This means that the measured orientation errors have very small fluctuations among the discrete points. The positioning performance of the robot, namely, their accuracy, is defined in accordance to ISO 9283: 1998 [23] as

$$AP_p = \delta p, AP_\phi = \delta\phi \tag{24}$$

where δp and $\delta\phi$ are the measured pose errors defined in Sec. 5.2. Figure 14 shows the accuracy of the manipulator, where the measured points covering the maximum workspace are demonstrated in Fig. 12(*a*). The position accuracy in measured points is $0.2 - 0.35$mm, while the orientation accuracy is $0.2 - 0.45$deg.

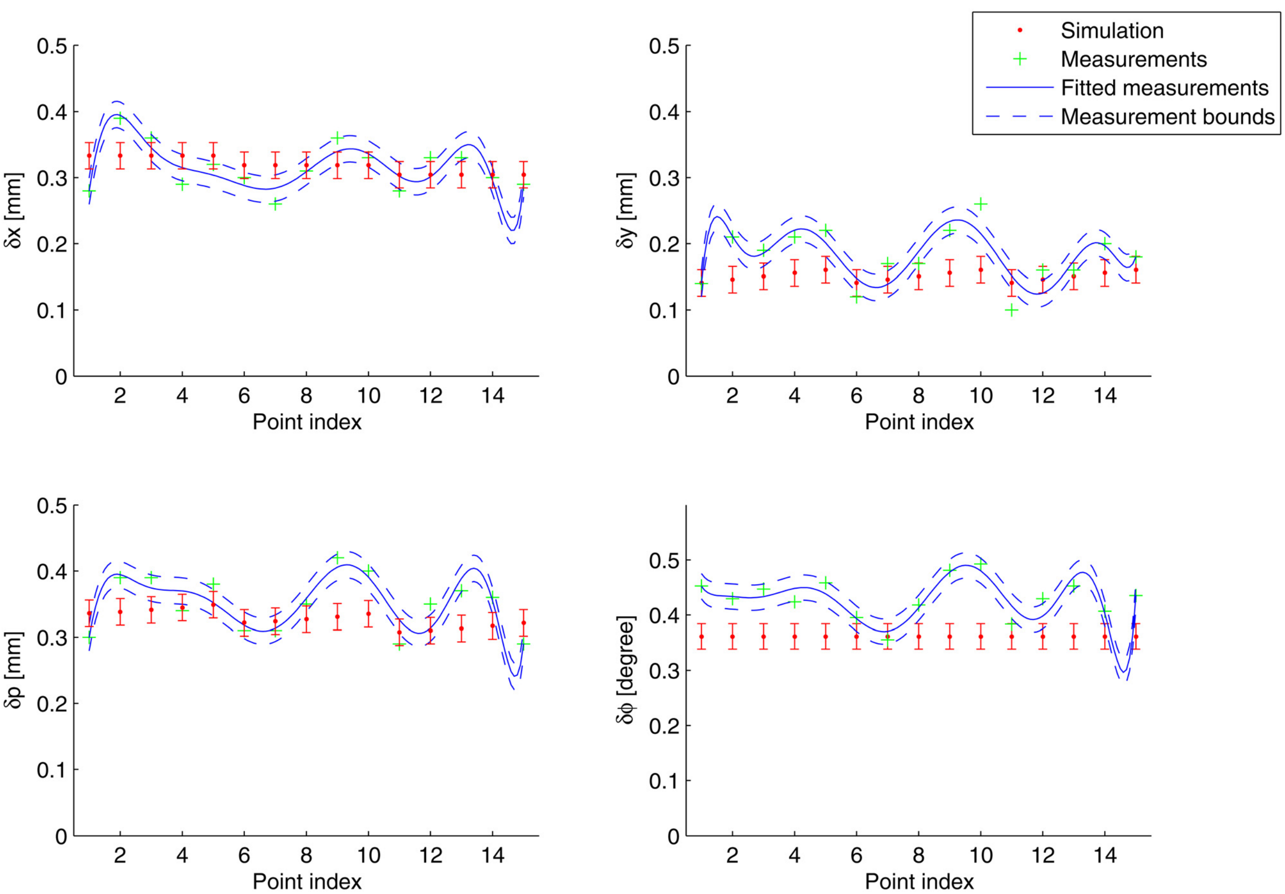

Fig. 15 Comparison between the measurements and simulation results for case 2 with a constant orientation $\phi = \pi/6$

The experiments show that most of the measurements line along the boundaries established with the mathematical model, with a few exceptions. In order to evaluate the comparison between the simulations and measurements, we made a statistical regression analysis [24], as shown in Fig. 15 for case 2 with a constant orientation $\phi = \pi/6$. Most of the simulation results are distributed in the measured error bands $\delta_{\mathrm{mea}} \pm 2A_{\mathrm{mea}}$ except the orientation errors, where δ_{mea} is the measurement error defined in Sec. 5.2 and A_{mea} is the accuracy of the measurement system in Sec. 5. The deviations in the simulation results are equal to 0.02 mm and 0.023 deg, respectively, as derived from the measurements of joint clearances. Although the simulated $\delta\phi$ are located beyond the measured error band for some points, the maximum difference between the two error bands is 0.086 deg, which means that the simulation results are quite close to the measurements. The possible reasons which cause disagreement between the simulations and measurements are random and systematic errors, the influence of the MP inclination and elastic deflection, etc.

7 Conclusions

In this paper, the pose error of a planar parallel manipulator was studied. A new error model was developed for PPMs with due considerations of both configuration errors and joint clearances. With the model, the pose error estimation problem was formulated as an optimization problem, which can estimate maximum pose errors. The error analysis method was deduced and explained in detail. This method can also be applied to planar serial mechanisms.

Another contribution lies in the experimental validation of the error model. Experiments were conducted to obtain the distribution of pose errors throughout the workspace, the results being compared with the errors estimated by the error model. It turns out that there is a good correlation between the pose error simulations and measurements. Moreover, the simulations show that the angular clearances in the passive prismatic joints have much more influence on the pose errors of the moving platform than the revolute joint clearances. This is associated with the experiments, in which the angular clearances in the linear bearings reach their tolerance bounds as much as possible. This suggests that one possible approach to eliminate the errors due to joint clearances is to preload the joint. The validated work can be used for error analysis and compensation in future work. Moreover, other error sources such as manufacturing errors will be considered.

Nomenclature

AP_p, AP_ϕ = position and orientation accuracy of the manipulator

$\Delta\rho_i, \varepsilon_{ri}$ = radial displacement at the ith revolute joint due to clearance and its tolerance

$\Delta\sigma_{gi}, \varepsilon_g$ = lateral displacement at the ith actuated prismatic joint (linear guide) due to clearance and its tolerance

$\Delta\tau_{bi}, \varepsilon_{\theta i}$ = angular displacement at the ith passive prismatic joint (linear bearing) due to clearance and its tolerance

$\Delta\tau_{gi}$ = angular displacement at the ith actuated prismatic joint (linear guide) due to clearance

$\boldsymbol{\delta}^c_{\mathrm{var}}$ = the vector of joint clearances

$\boldsymbol{\delta}_{\mathrm{var}}$ = the vector of variations in all design parameters

$\delta a_{ix}, \delta a_{iy}(\delta b_{ix}, \delta b_{iy}, \delta c_{ix}, \delta c_{iy}, \delta d_{ix}, \delta d_{iy})$ = variations in the Cartesian coordinates of point $A_i(B_i, C_i, D_i)$

$\delta x, \delta y$ = MP positioning errors along x- and y-axis

$\delta x^{ij}, \delta y^{ij}, \delta\phi^{ij}, \delta p^{ij}$ = measured values of x, y, orientation and positioning errors of the MP at the (i, j)th measurement point

$\delta x_{\max}, \delta y_{\max}, \delta\phi_{\max}, \delta p_{\max}$ = simulated maximum values of x, y, orientation and positioning errors of the MP

$\mathbf{A}, \mathbf{B}$ = forward and backward kinematic Jacobian matrices

$\mathbf{J}^c_{\mathrm{err}}$ = sensitivity Jacobian matrix to joint clearances

$\mathbf{J}_{\mathrm{err}}$ = global sensitivity Jacobian matrix

$\mathbf{p}, \delta\mathbf{p}$ = Cartesian coordinates vector of point P and its variations

$\phi, \delta\phi$ = orientation of the moving platform and its variation

$l_i, \delta l_i$ = displacement of the ith passive prismatic joint and its variation

$s_i, \delta s_i$ = displacement of the ith actuated prismatic joint and its variation

$\mathcal{F}_b(O, x, y)$ = base coordinate frame

$\mathcal{F}_p(P, X, Y)$ = coordinate frame attached to moving platform

Appendix

The matrices in Eq. (9) are given below

$$\mathbf{H}_a = \mathrm{diag}\left[\mathbf{w}_1^T\mathbf{E}^T\mathbf{h}_1 \quad \mathbf{w}_2^T\mathbf{E}^T\mathbf{h}_2 \quad \mathbf{w}_3^T\mathbf{E}^T\mathbf{h}_3\right] \tag{A1a}$$

$$\mathbf{H}_\alpha = \mathrm{diag}\left[\mathbf{w}_1^T(a_1\mathbf{h}_1 + s_1\mathbf{u}_1 + d_1\mathbf{v}_1) + l_1 \ \mathbf{w}_2^T(a_2\mathbf{h}_2 + s_2\mathbf{u}_2 + d_2\mathbf{v}_2) + l_2 \ \mathbf{w}_3^T(a_3\mathbf{h}_3 + s_3\mathbf{u}_3 + d_3\mathbf{v}_3) + l_3\right] \tag{A1b}$$

$$\mathbf{H}_\beta = \mathrm{diag}\left[\mathbf{w}_1^T(s_1\mathbf{u}_1 + d_1\mathbf{v}_1) + l_1 \quad \mathbf{w}_2^T(s_2\mathbf{u}_2 + d_2\mathbf{v}_2) + l_2 \quad \mathbf{w}_3^T(s_3\mathbf{u}_3 + d_3\mathbf{v}_3) + l_3\right] \tag{A1c}$$

$$\mathbf{H}_d = \mathrm{diag}\left[\mathbf{w}_1^T\mathbf{E}^T\mathbf{v}_1 \quad \mathbf{w}_2^T\mathbf{E}^T\mathbf{v}_2 \quad \mathbf{w}_3^T\mathbf{E}^T\mathbf{v}_3\right] \tag{A1d}$$

$$\mathbf{H}_\gamma = \mathrm{diag}\left[d_1\mathbf{w}_1^T\mathbf{v}_1 + l_1 \quad d_2\mathbf{w}_2^T\mathbf{v}_2 + l_2 \quad d_3\mathbf{w}_3^T\mathbf{v}_3 + l_3\right] \tag{A1e}$$

$$\mathbf{H}_\theta = \mathrm{diag}\left[l_1 \quad l_2 \quad l_3\right] \tag{A1f}$$

$$\mathbf{H}_\rho = \mathrm{diag}\left[\mathbf{w}_1^T\mathbf{E}^T\mathbf{n}_1 \quad \mathbf{w}_2^T\mathbf{E}^T\mathbf{n}_2 \quad \mathbf{w}_3^T\mathbf{E}^T\mathbf{n}_3\right] \tag{A1g}$$

$$\mathbf{H}_r = \mathrm{diag}\left[\mathbf{w}_1^T\mathbf{E}^T\mathbf{k}_1 \quad \mathbf{w}_2^T\mathbf{E}^T\mathbf{k}_2 \quad \mathbf{w}_3^T\mathbf{E}^T\mathbf{k}_3\right] \tag{A1h}$$

$$\mathbf{H}_\psi = \mathrm{diag}\left[r_1\mathbf{w}_1^T\mathbf{k}_1 \quad r_2\mathbf{w}_2^T\mathbf{k}_2 \quad r_3\mathbf{w}_3^T\mathbf{k}_3\right] \tag{A1i}$$

The matrices $\mathbf{J}_A, \mathbf{J}_B, \mathbf{J}_C$, and $\mathbf{J}_D$ in Eq. (13) are expressed as

$$\mathbf{J}_A = [\mathbf{J}_a \quad \mathbf{J}_\alpha][\mathbf{A}_a \quad \mathbf{A}_\alpha]^{-1}_{6\times 6}, \mathbf{A}_a = \mathrm{diag}[\mathbf{h}_1 \quad \mathbf{h}_2 \quad \mathbf{h}_3], \mathbf{A}_\alpha = \mathrm{diag}[a_1\mathbf{E}\mathbf{h}_1 \quad a_2\mathbf{E}\mathbf{h}_2 \quad a_3\mathbf{E}\mathbf{h}_3] \tag{A2a}$$

$$\mathbf{J}_B = [\mathbf{0}_{3\times 3} \quad \mathbf{J}_\beta][\mathbf{B}_s \quad \mathbf{B}_\beta]^{-1}_{6\times 6}, \mathbf{B}_s = \mathrm{diag}[\mathbf{u}'_1 \quad \mathbf{u}'_2 \quad \mathbf{u}'_3], \mathbf{B}_\beta = \mathrm{diag}[s_1\mathbf{E}\mathbf{u}'_1 \quad s_2\mathbf{E}\mathbf{u}'_2 \quad s_3\mathbf{E}\mathbf{u}'_3] \tag{A2b}$$

$$\mathbf{J}_C = [\mathbf{J}_d \quad \mathbf{J}_\gamma][\mathbf{C}_d \quad \mathbf{C}_\gamma]^{-1}_{6\times 6}, \mathbf{C}_d = \mathrm{diag}[\mathbf{v}'_1 \quad \mathbf{v}'_2 \quad \mathbf{v}'_3], \mathbf{C}_\gamma = \mathrm{diag}[d_1\mathbf{E}\mathbf{v}'_1 \quad d_2\mathbf{E}\mathbf{v}'_2 \quad d_3\mathbf{E}\mathbf{v}'_3] \tag{A2c}$$

$$\mathbf{J}_D = [\mathbf{J}_r \quad \mathbf{J}_\psi][\mathbf{D}_r \quad \mathbf{D}_\psi]^{-1}_{6\times 6}, \mathbf{D}_r = \mathrm{diag}[\mathbf{k}'_1 \quad \mathbf{k}'_2 \quad \mathbf{k}'_3], \mathbf{D}_\psi = \mathrm{diag}[r_1\mathbf{E}\mathbf{k}'_1 \quad r_2\mathbf{E}\mathbf{k}'_2 \quad r_3\mathbf{E}\mathbf{k}'_3] \tag{A2d}$$

with

$$\mathbf{u}'_i = \begin{bmatrix} \cos\beta_i \\ \sin\beta_i \end{bmatrix}, \mathbf{v}'_i = \begin{bmatrix} \cos\gamma_i \\ \sin\gamma_i \end{bmatrix}, \mathbf{k}'_i = \begin{bmatrix} \cos\psi_i \\ \sin\psi_i \end{bmatrix}$$

References

[1] Ryu, J., and Cha, J., 2003, "Volumetric Error Analysis and Architecture Optimization for Accuracy of HexaSlide Type Parallel Manipulators," Mech. Mach Theory, **38**, pp. 227–240.

[2] Liu, H., Huang, T., and Chetwynd, D. G., 2011, "A General Approach for Geometric Error Modeling of Lower Mobility Parallel Manipulators," ASME J. Mech. Rob., **3**(2), 021013.

[3] Yu, A., Bonev, I. A., and Murray, P. Z., 2008, "Geometric Approach to the Accuracy Analysis of a Class of 3-DOF Planar Parallel Robots," Mech. Mach. Theory, **43**, pp. 364–375.

[4] Briot, S., and Bonev, I. A., 2010, "Accuracy Analysis of 3T1R Fully-Parallel Robots," Mech. Mach. Theory, **45**, pp. 695–706.

[5] Lin, P. D., and Chen, J. F., 1992, "Accuracy Analysis of Planar Linkages by the Matrix Method," Mech. Mach. Theory, **35**, pp. 507–516.

[6] Ting, K., Zhu, J., and Watkins, D., 2000, "The Effects of Joint Clearance on Position and Orientation Deviation of Linkages and Manipulators," Mech. Mach. Theory, **35**, pp. 391–401.

[7] Fogarasy, A., and Smith, M., 1998, "The Influence of Manufacturing Tolerance on the Kinematic Performance of Mechanisms," Proc. Inst. Mech. Eng. Part C: Mech. Eng. Sci., **212**, pp. 35–47.

[8] Lim, S. R., Kang, K., Park, S., Choi, W. C., Jae-Bok, S., Hong, D., and Shim, J. K., 2002, "Error Analysis of a Parallel Mechanism Considering Link Stiffness and Joint Clearances," J. Mech. Sci. Technol., **16**(6), pp. 799–809.

[9] Castelli, V. P., and Venanzi, S., 2005, "Clearance Influence Analysis on Mechanisms," Mech. Mach. Theory, **40**, pp. 1316–1329.

[10] Venanzi, S., and Castelli, V. P., 2005, "A New Technique for Clearance Influence Analysis in Spatial Mechanisims," ASME J. Mech. Des., **127**, pp. 446–455.

[11] Meng, J., Zhang, D., and Li, Z., 2009, "Accuracy Analysis of Parallel Manipulators With Joint Clearance," ASME J. Mech. Des., **131**, 011013.

[12] Binaud, N., Cardou, P., Caro, S., and Wenger, P., 2010, "The Kinematic Sensitivity of Robotic Manipulators to Joint Clearance," Proceedings of ASME Design Engineering Technical Conferences, Aug. 15–18, Montreal, QC, Canada.

[13] Binaud, N., Caro, S., Bai, S., and Wenger, P., 2010, "Comparison of 3-PPR Parallel Planar Manipulators Based on Their Sensitivity to Joint Clearances," Proceedings of IEEE/RSJ International Conference on Intelligent Robots and Systems (IROS), Taipei, Oct. 18–22, pp. 2778–2783.

[14] Wei, W., and Simaan, N., 2010, "Design of Planar Parallel Robots With Preloaded Flexures for Guaranteed Backlash Prevention," ASME J. Mech. Rob., **2**(1), 011012.

[15] Carusone, J., and D'Eleuterio, G. M., 1993, "Tracking Control for End-Effector Position and Orientation of Structurelly Flexible Manipulators," J. Rob. Syst., **10**(6), pp. 847–870.

[16] Zhuang, H., 1997, "Self-Calibration of Parallel Mechanisms With a Case Study on Stewart Platforms," IEEE Trans. Rob. Autom., **13**(3), pp. 387–397.

[17] Voglewede, P., and Uphoff, I., 2004, "Application of Workspace Generation Techniques to Determine the Unconstrained Motion of Parallel Manipulators," ASME J. Mech. Des., **126**, pp. 283–290.

[18] Bai, S., and Caro, S., 2009, "Design and Analysis of a 3-PPR Planar Robot With U-Shape Base," Proceedings of 14th International Conference on Advanced Robotics, Munich, Germany, June 22–26.

[19] SMAC Product Catalog version 2009 on the WWW, at http://www.smac-mca.com/

[20] Caro, S., Binaud, N., and Wenger, P., 2009, "Sensitivity Analysis of 3-R$\underline{\text{P}}$R Planar Parallel Manipulators," J. Mech. Des., **131**, 121005.

[21] http://www.pdfsupply.com/pdfs/dvt-554c.pdf

[22] http://www.cognex.com/support/files/DVT/Intellect_Manual.pdf

[23] International Standard, Manipulating Industrial Robots-Performance Criteria and Related Test Methods, ISO 9283: 1998.

[24] Douglas, C. M., 2009, *Design and Analysis of Experiments*, 7th ed., John Wiley & Sons.